Draft version October 7, 2005
Preprint typeset using LaTeX style emulateapj v. 6/22/04



# MULTI-DIMENSIONAL RADIATION/HYDRODYNAMIC SIMULATIONS OF PROTONEUTRON STAR CONVECTION

L. Dessart[1], A. Burrows[1], E. Livne[2], C.D. Ott[3]

*Draft version October 7, 2005*

## ABSTRACT

Based on multi-dimensional multi-group radiation hydrodynamic simulations of core-collapse supernovae with the VULCAN/2D code, we study the physical conditions within and in the vicinity of the nascent protoneutron star (PNS). Conclusions of this work are threefold: First, as before, we do not see any large-scale overturn of the inner PNS material. Second, we see no evidence of doubly-diffusive instabilities in the PNS, expected to operate on diffusion timescales of at least a second, but instead observe the presence of convection, within a radius range of 10-20 km, operating with a timescale of a few milliseconds. Third, we identify unambiguously the presence of gravity waves, predominantly at 200-300 milliseconds (ms) past core bounce, in the region separating the convective zones inside the PNS and between the PNS surface and the shocked region.

Our numerical study is an improvement over past work in a number of ways: we follow the evolution of the collapsing envelope from ∼200 ms before bounce to ∼500 ms after bounce; the spatial grid switches from Cartesian inside to spherical outside, permitting a handling of the inner PNS region at good spatial resolution, all the way inside to the center, and without severe Courant-time limitation; neutrino-transport is treated with a Multi-Group, Flux-Limited-Diffusion (MGFLD) approach, well suited for the study of the PNS, *i.e.*, in regions where the neutrino mean-free-path is small. With this configuration, VULCAN/2D has the ability to simulate doubly-diffusive instabilities, if present.

Convection, directly connected to the PNS, is found to occur in two distinct regions: between 10 and 20 km, coincident with the region of negative lepton gradient, and exterior to the PNS above 50 km. These two regions are separated by an interface, which shows no sizable outward or inward motion and efficiently shelters the inner PNS. The PNS is also the site of gravity waves, excited by the convection in the outer convective zone.

In the PNS, convection is always confined to a region between 10 and 20 km, *i.e.*, within the neutrinospheric radii for all neutrino energies above just a few MeV. We find that such motions do not appreciably enhance the $\nu_e$ neutrino luminosity, and that they can enhance the $\bar{\nu}_e$ and "$\nu_\mu$" luminosities by no more than ∼15% and ∼30%, respectively, during the first post-bounce ∼100 ms, after which the optical depth barrier between the inner convection and the neutrinospheres effectively isolates one from the other, terminating even this modest enhancement. PNS convection is thus found to be a secondary feature of the core-collapse phenomenon, rather than a decisive ingredient for a successful explosion.

Furthermore, the typical timescale associated with such convective transport is of the order of a few milliseconds, and thus is at least a thousand times faster than typical growth rates for instabilities associated with neutrino-mediated thermal and lepton diffusion. Such doubly-diffusive instabilities are, therefore, unlikely to play a substantial role in the early critical phases of the PNS. We conclude that inner PNS motions do not bear importantly on the potential success of core-collapse supernovae explosions.

*Subject headings:* convection – hydrodynamics – neutrinos – stars: neutron – stars: supernovae: general – waves

## 1. INTRODUCTION

A few million years after the onset of core-hydrogen burning on the main sequence, a massive star creates a degenerate core, which, upon reaching the Chandrasekhar mass, undergoes gravitational collapse. The core infall is eventually halted when its innermost regions reach nuclear densities, generating a shock wave that propagates outwards, initially reversing inflow into outflow. However, detailed numerical radiation-hydrodynamics simulations struggle to produce explosions. Instead of a prompt explosion occurring on a dynamical timescale, simulations produce a stalled shock at ∼100-200 km, just a few tens of milliseconds after core bounce: 1D simulations universally yield a stalled shock that ultimately fails to lift off; 2D simulations provide a more divided picture, with success or failure seemingly dependent on the numerical approach or physical assumptions made. Indeed, energy deposition by neutrinos behind the shock, in the so-called gain region, is expected to play a central role in re-energizing the stalled shock: explosion will occur if the shock can be maintained at large-enough radii and for a sufficiently long time to eventually expand into the tenuous infalling en-

[1] Department of Astronomy and Steward Observatory, The University of Arizona, Tucson, AZ 85721; luc@as.arizona.edu,burrows@as.arizona.edu
[2] Racah Institute of Physics, The Hebrew University, Jerusalem, Israel; eli@frodo.fiz.huji.ac.il
[3] Max-Planck-Institut für Gravitationsphysik, Albert-Einstein-Institut, Golm/Potsdam, Germany; cott@aei.mpg.de

velope (Burrows & Goshy 1993). At present, the failure to produce explosions may be due to physical processes not accounted for (e.g., magnetic fields), to an inaccurate treatment of neutrino transport (see the discussion in Buras et al. 2005), or to missing neutrino microphysics.

Because neutrino transport is a key component of the supernovae mechanism in massive stars, slight modifications in the neutrino cooling/heating efficiency could be enough to produce an explosion. Alternatively, an enhancement in the neutrino flux during the first second following core bounce could also lead to a successful explosion. Convection in the nascent protoneutron star (PNS) has been invoked as a potential mechanism for such an increase in the neutrino luminosity. Neutrino escape at and above the neutrinosphere establishes a negative lepton-gradient, a situation unstable to convection under the Ledoux (1947) criterion. Epstein (1979) argued, based on a simulation by Mayle & Wilson (1988), that this leads to large-scale overturn and advection of core regions with high neutrino-energy density at and beyond the neutrinosphere, thereby enhancing the neutrino flux. Such large scale overturn was obtained in simulations by Bruenn, Buchler & Livio (1979) and Livio, Buchler & Colgate (1979), but, as shown by Smarr et al. (1981), their results were compromised by an inadequate equation of state (EOS). Lattimer & Mazurek (1981) challenged the idea of large-scale overturn, noting the presence of a positive, stabilizing entropy gradient - a residue of the shock birth. Thus, while large-scale overturn of the core is unlikely and has thus far never been seen in realistic simulations of core-collapse supernovae, the possibility of convectively-enhanced neutrino luminosities was still open. Burrows (1987), based on a simple mixing-length treatment, argued that large-scale core-overturn was unlikely, but found neutrino-luminosity enhancements, stemming from convective motions within the PNS, of up to 50%. Subsequently, based on multi-dimensional (2D) radiation hydrodynamics simulations, Burrows, Hayes, & Fryxell (1995) did not find large-scale core overturn, nor any luminosity enhancement, but clearly identified the presence of convection within the PNS, as well as "tsunamis" propagating at its surface. Keil, Janka, & Müller (1996), using a similar approach, reported the presence of both convection and enhancement of neutrino luminosities compared to an equivalent 1D configuration. However, these studies used gray neutrino transport, a spherically-symmetric (1D) description of the inner core (to limit the Courant timestep), and a restriction of the angular coverage to 90°. Keil et al. also introduced a diffusive and moving outer boundary at the surface of the PNS (receding from 60 km down to 20 km, 1 s after core bounce), thereby neglecting any feedback from the fierce convection occurring above, between the PNS surface and the shock radius. Recently, Swesty & Myra (2005ab) described simulations of the convective epoch in core-collapse supernovae, using MGFLD neutrino transport, but their 2D study covers only the initial 33 milliseconds (ms) of PNS evolution.

Alternatively, Mayle & Wilson (1988) and Wilson & Mayle (1993) have argued that regions stable to convection according to the Ledoux criterion could be the sites of doubly-diffusive instabilities, taking the form of so-called neutron (low-$Y_e$ material) fingers. This idea rests essentially on the assumption that the neutrino-mediated diffusion of heat occurs on shorter timescales than the neutrino-mediated diffusion of leptons. By contrast, Bruenn & Dineva (1996) and Bruenn, Raley, & Mezzacappa (2005) demonstrated that the neutrino-mediated thermal-diffusion timescale is longer than that of neutrino-mediated lepton-diffusion, and, thus, that neutron fingers do not obtain. Because $\nu_\mu$'s and $\nu_\tau$'s have a weak thermal coupling to the material, Bruenn, Raley, & Mezzacappa (2005) concluded that lepton-diffusion would occur faster by means of low-energy $\bar{\nu}_{\rm e}$'s and $\nu_{\rm e}$'s. Applying their transport simulations to snapshots of realistic core-collapse simulations, they identified the potential for two new types of instabilities within the PNS, referred to as "lepto-entropy fingers" and "lepto-entropy semiconvection."

In this paper, we present a set of simulations that allow a consistent assessment of dynamical/diffusive/convective mechanisms taking place within the PNS, improving on a number of assumptions made by previous radiation-hydrodynamic investigations. Our approach, based on VULCAN/2D (Livne et al. 2004), has several desirable features for the study of PNS convection. First, the 2D evolution of the inner 3000-4000 km of the core-collapsing massive star is followed from pre-bounce to post-bounce. Unlike other groups (Janka & Müller 1996; Swesty & Myra 2005ab), we do not start the simulation at post-bounce times by remapping a 1D simulation evolved till core bounce. Second, the VULCAN/2D grid, by switching from Cartesian (cylindrical) in the inner region (roughly the central 100 km$^2$) to spherical above ∼20 km, allows us to maintain good resolution, while preventing the Courant timestep from becoming prohibitively small. Additionally, this grid naturally permits the core to move and, thus, in principle, provides a consistent means to assess the core recoil associated with asymmetric explosions. Third, the large radial extent of the simulation, from the inner core to a few thousand km, allows us to consider the feedback effects between different regions. Fourth, our use of Multi-Group Flux-Limited Diffusion is also particularly suited for the analysis of mechanisms occurring within a radius of 50 km, since there, neutrinos have a diffusive behavior, enforced by the high opacity of the medium at densities above $10^{11}\,{\rm g\,cm^{-3}}$. Fifth, lateral transport of neutrino energy and lepton number is accounted for explicitly, an asset over the more approximate ray-by-ray approach (Burrows, Hayes, & Fryxell 1995; Buras et al. 2005) which cannot simulate accurately the behavior of doubly-diffusive instabilities. A limitation of our work is the neglect of the subdominant inelastic $e^- - \nu_e$ scattering in this version of VULCAN/2D.

The present paper is structured as follows. In §2, we discuss the VULCAN/2D code on which all simulations studied here are based. In §3, we describe in detail the properties of our baseline model simulation, emphasizing the presence/absence of convection, and limiting the discussion to the inner 50-100 km. In §4, focusing on results from our baseline model, we characterize the PNS convection and report the lack of doubly-diffusive instabilities within the PNS. Additionally, we report the unambiguous presence of gravity waves, persisting over a few hundred milliseconds, close to the minimum in the electron-fraction distribution, at ∼20–30 km. In §5, we

conclude and discuss the broader significance of our results in the context of the mechanism of core-collapse supernovae.

## 2. VULCAN/2D AND SIMULATION CHARACTERISTICS

All radiation-hydrodynamics simulations presented in this paper were performed with a time-explicit variant of VULCAN/2D (Livne 1993), adapted to model the mechanism of core-collapse supernovae (Livne et al. 2004; Walder et al. 2005; Ott et al. 2004). The code uses cylindrical coordinates $(r, z)$ where $z$ is the distance parallel to the axis of symmetry (and, sometimes, the axis of rotation) and $r$ is the position perpendicular to it [4]. VULCAN/2D has the ability to switch from a Cartesian grid near the base to a spherical-polar grid above a specified radius: in all computations presented here, this transition takes place at ∼20 km (which embraces ∼85% of the total PNS mass at 500 ms). Outside of the Cartesian mesh, the baseline calculation employs 121 angular zones equally spaced over 180°, and allocates 162 radial shells between ∼20 km and the outer radius at 3800 km. To preserve a high resolution near the core as well as to limit the computational cost of our simulations, the radial increment increases logarithmically above 30 km, with $\Delta R_{\rm min}$ ∼1 km and $\Delta R_{\rm max}$ ∼125 km. Results presented in this paper may not be converged due to this relatively coarse resolution. As mentioned in §1, this flexible grid possesses two assets: the grid resolution is essentially uniform everywhere within 20 km from the center of the object, and, thus, does not impose a prohibitively small Courant timestep for our explicit hydrodynamic scheme, and the motion of the core is readily permitted, allowing estimates of potential core recoils resulting from global asymmetries in the fluid/neutrino momentum[5]. The inner PNS can be studied right down to the core of the objects since no artificial inner (reflecting) boundary is placed there (Burrows, Hayes, & Fryxell 1995; Janka & Müller 1996; Keil, Janka & Müller 1996; Swesty & Myra 2005ab). Along the axis, we use a reflecting boundary, while at the outer grid radius, we prevent any flow of material ($V_R = 0$), but allow the free-streaming of the neutrinos.

We simulate neutrino transport using a diffusion approximation in 2D, together with a 2D flux limiter (Bruenn 1985). To improve over previous gray transport schemes, we solve the transport at different neutrino energies using a coarse, but satisfactory, sampling at 16 energy groups equally spaced in the log between 1 and 200 MeV. We have also investigated the consequences of using a lower energy resolution, with only 8 energy groups, and for the PNS region we find no differences of a qualitative nature, and, surprisingly, few differences of a quantitative nature. While the neutrino energy distribution far above the neutrinosphere(s) (few 1000 km) has a thermal-like shape with a peak at ∼15 MeV and width of ∼10 MeV, deep in the nascent PNS, the distribution peaks beyond 100 MeV and is very broad. In other words, we use a wide range of neutrino energies to solve the transport in order to model absorption/scattering/emission relevant at the low energies exterior to the neutrinospheres, and at the high energies interior to the neutrinospheres.

In this investigation, we employ a single progenitor model, the 11 $M_\odot$ ZAMS model (s11) of Woosley & Weaver (1995); when mapped onto our Eulerian grid, at the start of the simulation, the 1.33 $M_\odot$ Fe-core, which stretches out to 1300 km, is already infalling. Hence, even at the start of the simulation, the electron fraction extends from 0.5 above the Fe core down to 0.43 at the center of the object.

Besides exploring the dependence on PNS convection of the number of energy groups, we have also investigated the effects of rotation. For a model with an initial inner rotational period of 10.47 seconds ($\Omega = 0.6$ rad s$^{-1}$), taken from Walder et al. (2005), and with a PNS spin period of 10 ms after ∼200 ms (Ott et al. 2005), we see no substantive differences with our baseline model. Hence, we have focused in this paper on the results from the non-rotating baseline model [6].

Finally, before discussing the results for the baseline model, we emphasize that the word "PNS" is to be interpreted loosely: we mean by this the regions of the simulated domain that are within a radius of ∼50 km. If the explosion fails, the entire progenitor mantle will eventually infall and contribute its mass to the compact object. If the explosion succeeds, it remains to be seen how much material will reach escape velocities. At 500 ms past core bounce, about 99% of the progenitor core mass is within 30 km.

## 3. DESCRIPTION OF THE RESULTS OF THE BASELINE MODEL

In this section, we present results from the baseline VULCAN/2D simulation, whose parameters and characteristics were described in §2. First, let us describe the gross properties of the simulation, covering the first 300 ms past core bounce and focusing exclusively on the inner 50–100 km. In Fig. 1–3, we show stills of the entropy (Fig. 1), electron fraction (Fig. 2), and density (Fig. 3) at 50 (top left panel), 100 (top right), 200 (bottom left), and 300 ms (bottom right) after core bounce. We also provide, in Fig. 4, radial cuts of a sample of quantities in the equatorial direction, to provide a clearer view of, for example, gradients. Overall, the velocity magnitude is in excess of 5000 km s$^{-1}$only beyond ∼50 km, while it is systematically below 2000 km s$^{-1}$within the same radius. At early times after bounce ($t = 50$ ms), the various plotted quantities are relatively similar throughout the inner 50 km. The material velocities are mostly radial, oriented inward, and very small, *i.e.*, do not exceed 1000–2000 km s$^{-1}$. The corresponding Mach numbers throughout the PNS are subsonic, not reaching more than ∼10% of the local sound speed. This rather quiescent structure is an artefact of the early history of the young PNS before vigorous dynamics ensues. The shock wave generated at core bounce, after the initial dramatic compression up to nuclear densities (∼$3\times10^{14}$ g cm$^{-3}$) of the inner progenitor regions, leaves a positive entropy gradient, reaching then its maximum of ∼6-7 $k_B$/baryon at ∼150 km, just below the shock. The electron fraction ($Y_e$) shows a broad minimum between ∼20 and ∼80 km,

[4] The spherical radius, $R$, is given by the quantity $\sqrt{r^2 + z^2}$.

[5] For a display of the grid morphology, see Fig. 4 in Ott et al. (2004).

[6] The consequences in the PNS core of much faster rotation rates will be the subject of a future paper.

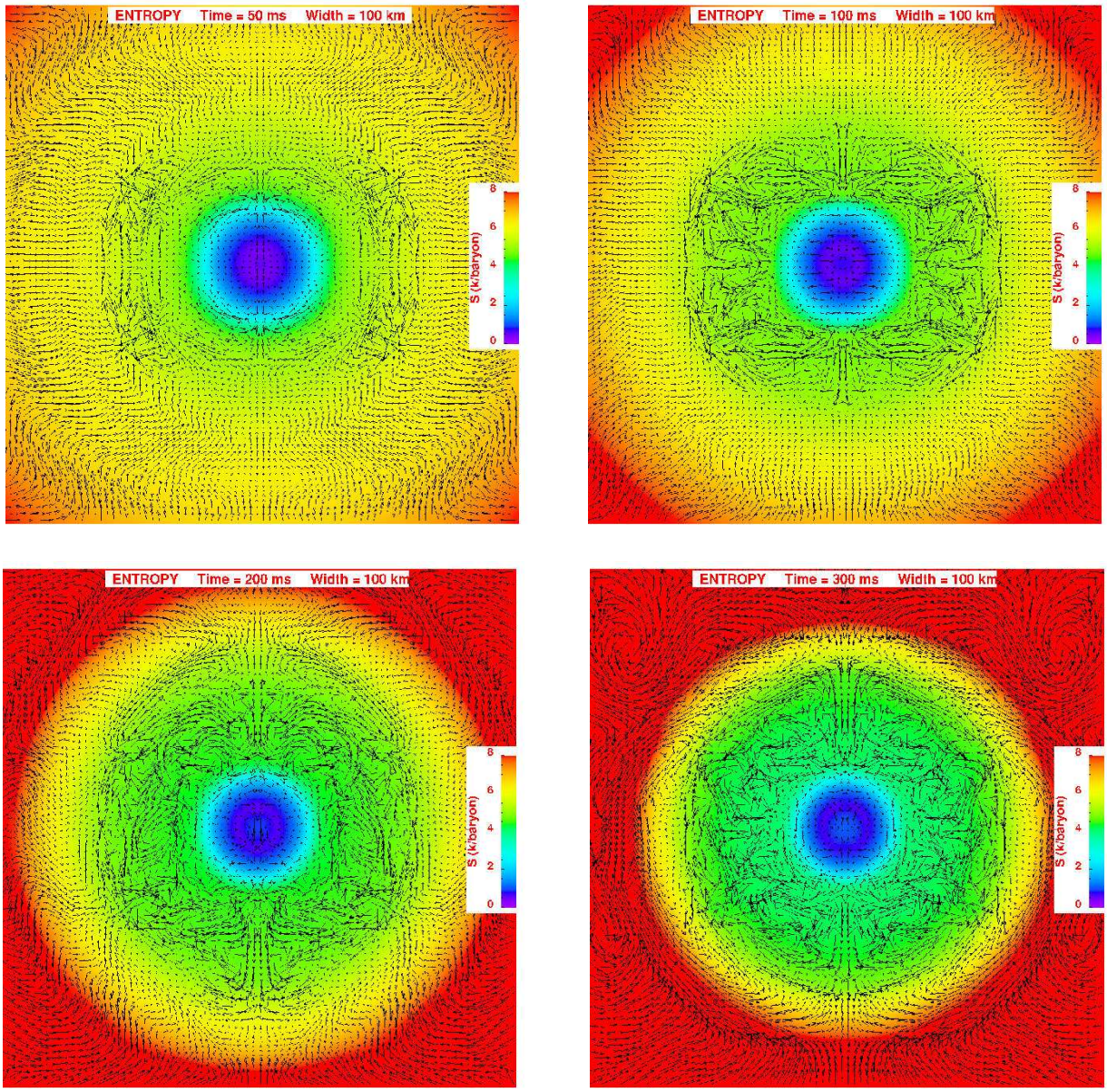


FIG. 1.— Color map stills of the entropy, taken at 50 (top left), 100 (top right), 200 (bottom left), and 300 ms (bottom right) past core bounce, with velocity vectors overplotted. Here "Width" refers to the diameter; the radius through the middle is 50 kilometers. Note that to ease the comparison between panels, the same range of values of the color map are used throughout (see text for discussion).

a result of the continuous deleptonization of the corresponding regions starting after the neutrino burst near core bounce. Within the innermost radii (∼10–20 km), the very high densities ($\geq 10^{12}\,\mathrm{g\,cm^3}$) ensure that the region is optically-thick to neutrinos, inhibiting their escape.

Turning to the next phase in our time series ($t = 100$ ms), we now clearly identify four zones within the inner 50 km, ordered from innermost to outermost, which will become increasingly distinct with time:

- Region A: This is the innermost region, within 10 km, with an entropy of $\sim 1\,k_B$/baryon, a $Y_e$ of 0.2–0.3, a density of $\sim$1-4$\times 10^{14}\,\mathrm{g\,cm^{-3}}$, essentially at rest with a near-zero Mach number (negligible vorticity and divergence). This region has not appreciably changed in the elapsed 50 ms, and will in fact not do so for the entire evolution described here.

- Region B: Between 10 and 30 km, we see a region of higher entropy (2–5 $k_B$/baryon) with positive-gradient and lower $Y_e$ with negative gradient (from $Y_e$ of ∼0.3 down to ∼0.1). Despite generally low Mach number, this region exhibits significant motions with pronounced vorticity, resulting from the unstable negative-gradient of the electron (lepton) fraction.

- Region C: Between 30 and 50 km is a region of outwardly-increasing entropy (5–8 $k_B$/baryon), but with a flat and low electron fraction; this is the most deleptonized region in the entire simulated object at this time. There, velocities are vanish-

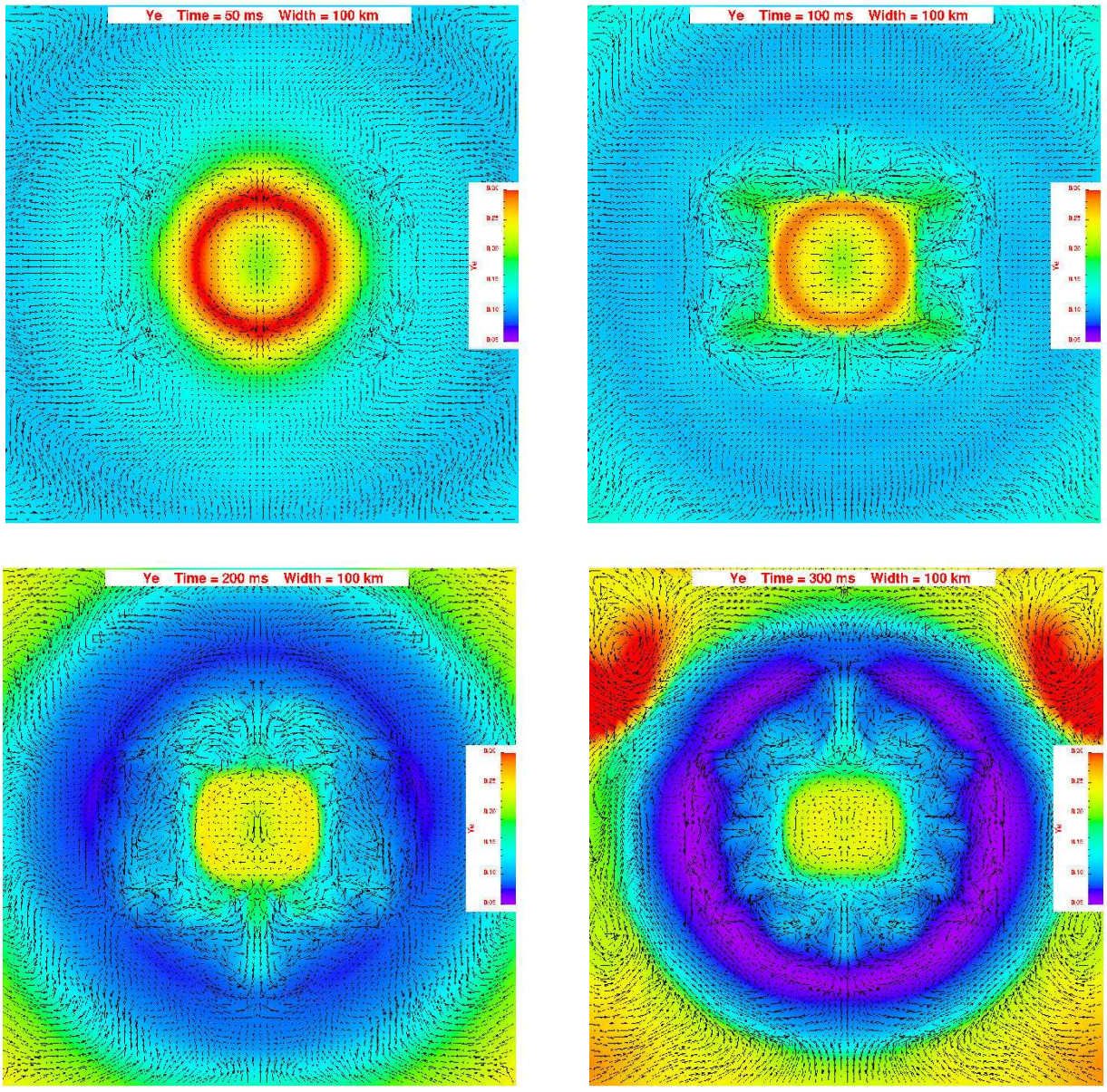


FIG. 2.— Same as Fig. 1, but for the electron fraction $Y_e$.

ingly small ($\ll 1000\,\mathrm{km\,s^{-1}}$), as in Region A, although generally oriented radially inwards. This is the cavity region where gravity waves are generated, most clearly at 200–300 ms in our time series.

- Region D: Above 50 km, the entropy is still increasing outward, with values in excess of $8\,k_B$/baryon, but now with an outwardly-increasing $Y_e$ (from the minimum of 0.1 up to 0.2). Velocities are much larger than those seen in Region B, although still corresponding to subsonic motions at early times. Negligible vorticity is generated at the interface between Regions C and D. The radially infalling material is prevented from entering Region C and instead settles on its periphery.

As time progresses, these four regions persist, evolving only slowly for the entire ∼300 ms after bounce. The electron fraction at the outer edge of Region A decreases. The convective motions in low–$Y_e$ Region B induce significant mixing of the high-$Y_e$ interface with Region A, smoothing the $Y_e$ peak at ∼10 km. Overall, Region A is the least changing region. In Region B, convective motions, although subsonic, are becoming more violent with time, reaching Mach numbers of ∼0.15 at 200 ms, and ∼0.2 (at 300 ms), associated with a complex flow velocity pattern. In Region C, the trough in electron fraction becomes more pronounced, reaching down to 0.1 at 200 ms, and a record-low of 0.05 at 300 ms. Just on its outer edge, one sees sizable (a few$\times 100\,\mathrm{km\,s^{-1}}$) and nearly-exclusively latitudinal motions, persisting over large angular scales. Region D has changed significantly, displaying low-density, large-scale structures with downward and upward velocities. These effectively couple remote regions, between the high-entropy, high–$Y_e$ shocked re-

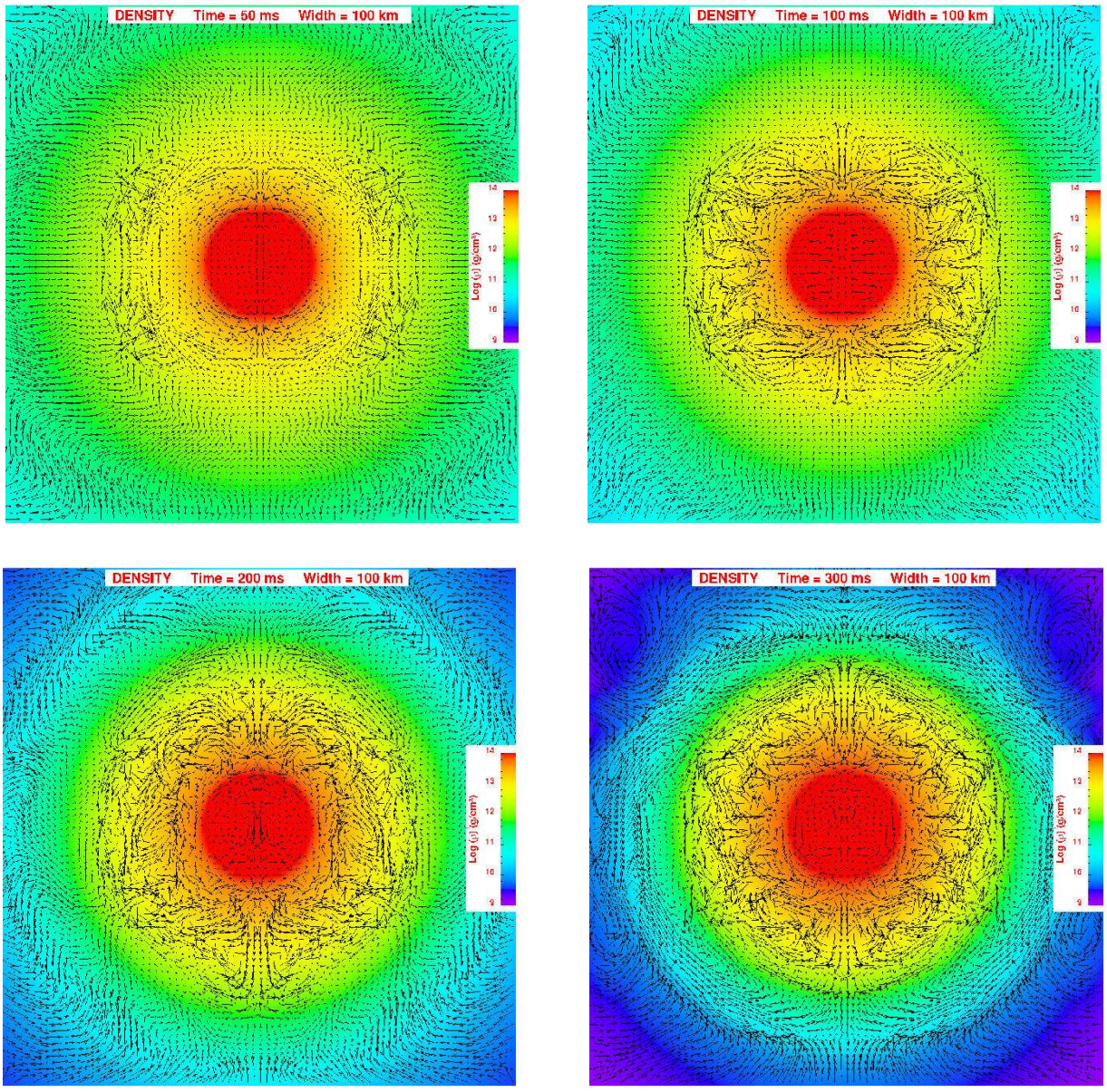


FIG. 3.— Same as Fig. 1, but for the mass density $\rho$.

gion and the low-entropy, low–$Y_e$ Region C. Region D also stretches further in (down to ∼45 km), at the expense of Region C which becomes more compressed. This buffer region C seems to shelter the interior, which has changed more modestly than region D.

Figure 4 shows radial cuts along the equator for the four time snapshots (black: 50 ms; blue: 100 ms; green: 200 ms; red: 300 ms) shown in Figs. 1-3 for the density (upper left), temperature (upper right), entropy (middle left), $Y_e$ (middle right), radial velocity (bottom left), and Mach number (bottom right). Notice how the different regions are clearly visible in the radial-velocity plot, showing regions of significant upward/downward motion around 20 km (Region B) and above ∼50 km (Region D). One can also clearly identify the $Y_e$ trough, whose extent decreases from 30–90 km at 50 ms to 30–40 km at 300 ms. The below-unity Mach number throughout the inner 50 km also argues for little ram pressure associated with convective motions in those inner regions. Together with the nearly-zero radial velocities in Regions A and C at all times, this suggests that of these three regions mass motions are confined to Region B.

One can identify a trend of systematic compression of Regions B–C–D, following the infall of the progenitor mantle. Indeed, despite the near-stationarity of the shock at 100–200 km over the first 200–300 ms, a large amount of mass flows inward through it, coming to rest at smaller radii. In Fig. 5, we display the evolution, up to 530 ms past core bounce (for a more extended view), of the interior mass and mass flow through different radial shells within the PNS. Note that mass inflow in this context has two components: 1) direct accretion of material from the infalling progenitor envelope and, 2) the compression of the PNS material as it cools and deleptonizes.

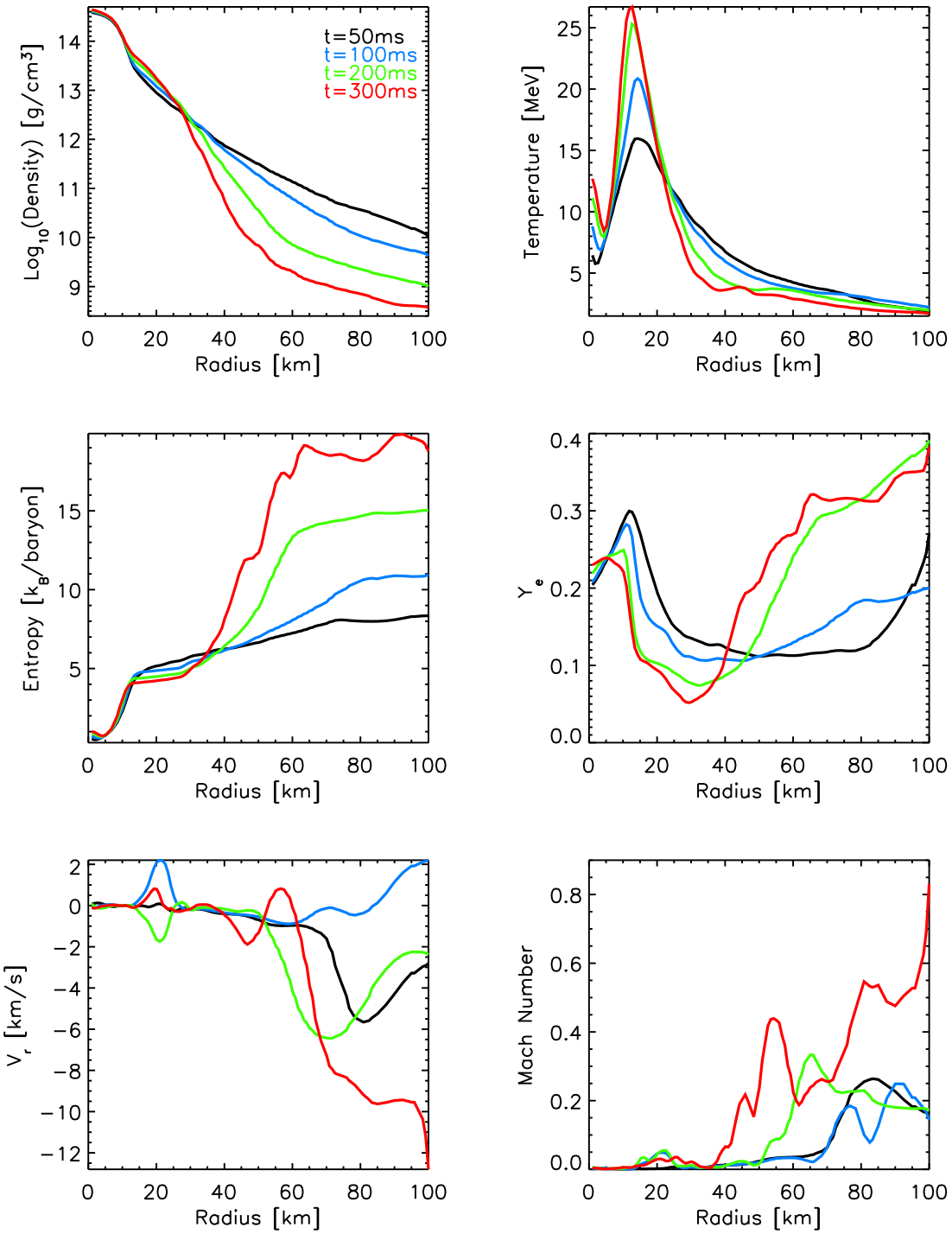


FIG. 4.— Montage of radial cuts along the equatorial direction at 50 (black), 100 (blue), 200 (green), and 300 ms (red) past core bounce, corresponding to the same sequence as Figs 1-3, for the density (top left), temperature (top right), entropy (middle left), $Y_e$ (middle right), radial velocity (bottom left), and Mach number (bottom right).

Hence, mass inflow through radial shells within the PNS would still be observed even in the absence of explicit accretion of material from the shock region. By 530 ms past core bounce, the "accretion rate" has decreased from a maximum of $\sim$ 1-3 $M_\odot\,s^{-1}$ at 50 ms down to values below $0.1\,M_\odot\,s^{-1}$ and the interior mass at 30 km has stabilized to $\sim 1.4\,M_\odot$. Interestingly, the mass flux at a radius of 20 km is lower (higher) at early (late) times compared to that in the above layers, and remains non-negligible even at 500 ms.

An instructive way to characterize the properties of the fluid within the PNS is by means of Distribution Functions (DFs), often employed for the description of the solar convection zone (Browning, Brun, & Toomre 2004).

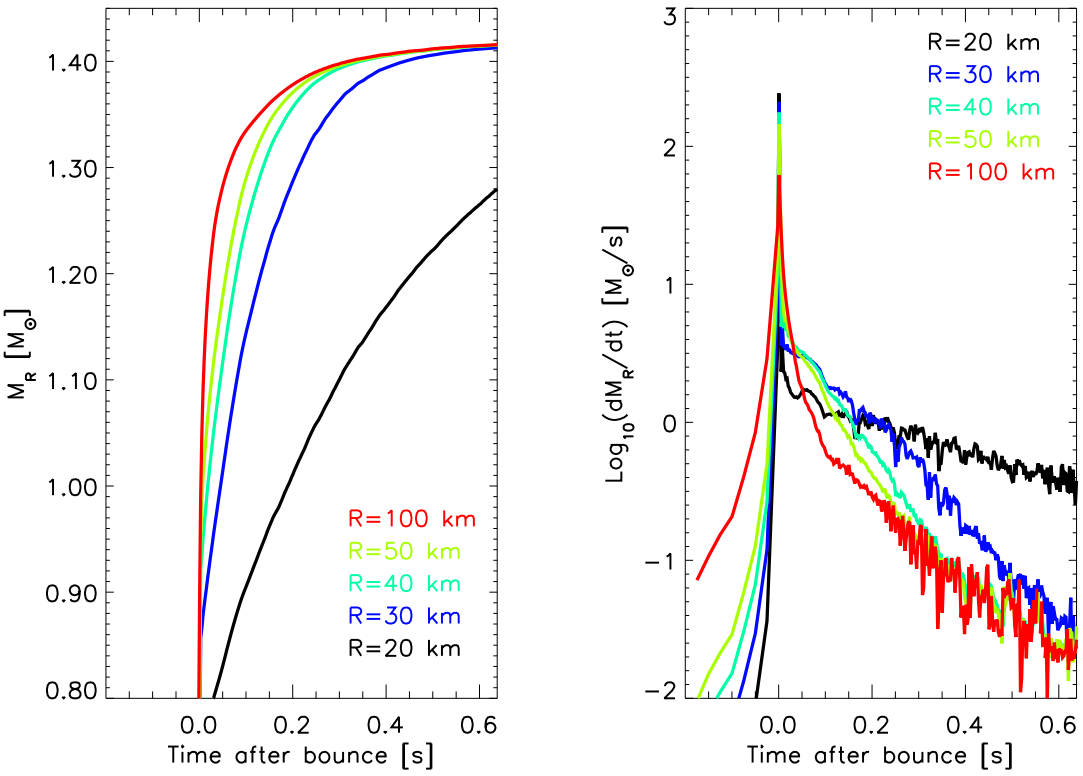


FIG. 5.— *Left*: Time evolution after bounce of the interior mass spherical shells at selected radii: 20 km (black), 30 km (blue), 40 km (red) and 50 km (black). *Right*: Corresponding mass flow through the same set of radii.

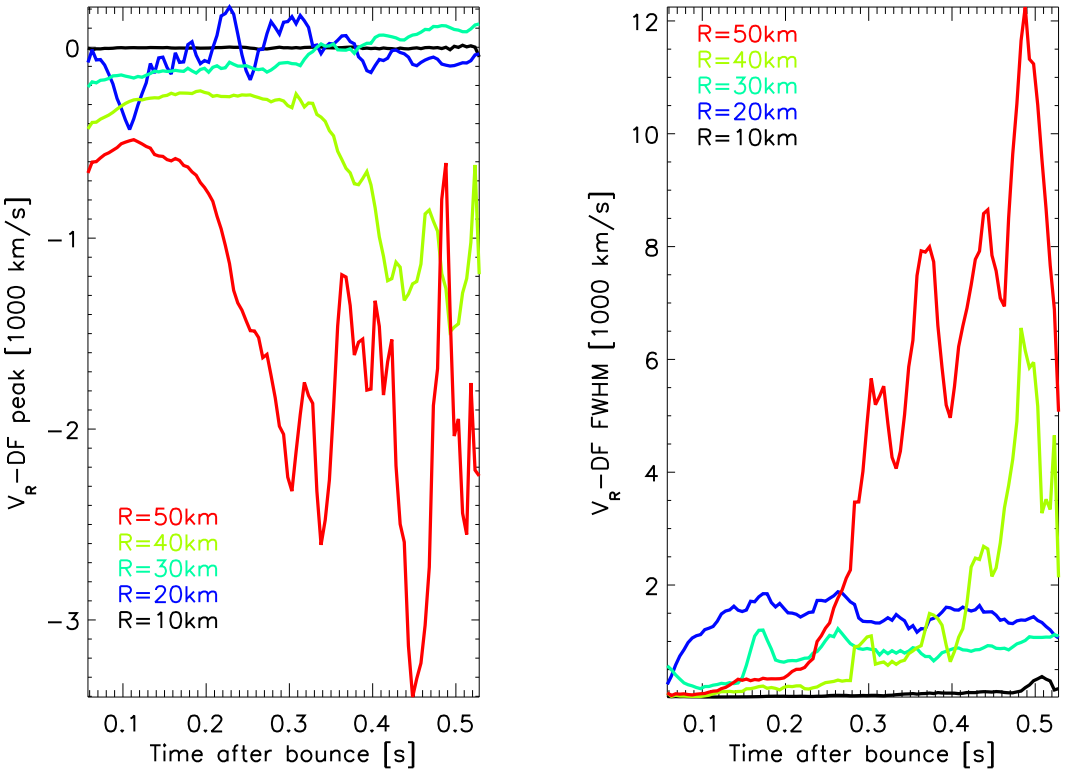


FIG. 6.— Time evolution, at selected radii, of the radial-velocity at peak and Full Width at Half Maximum (FWHM) of the radial-velocity distribution function. See text for discussion.

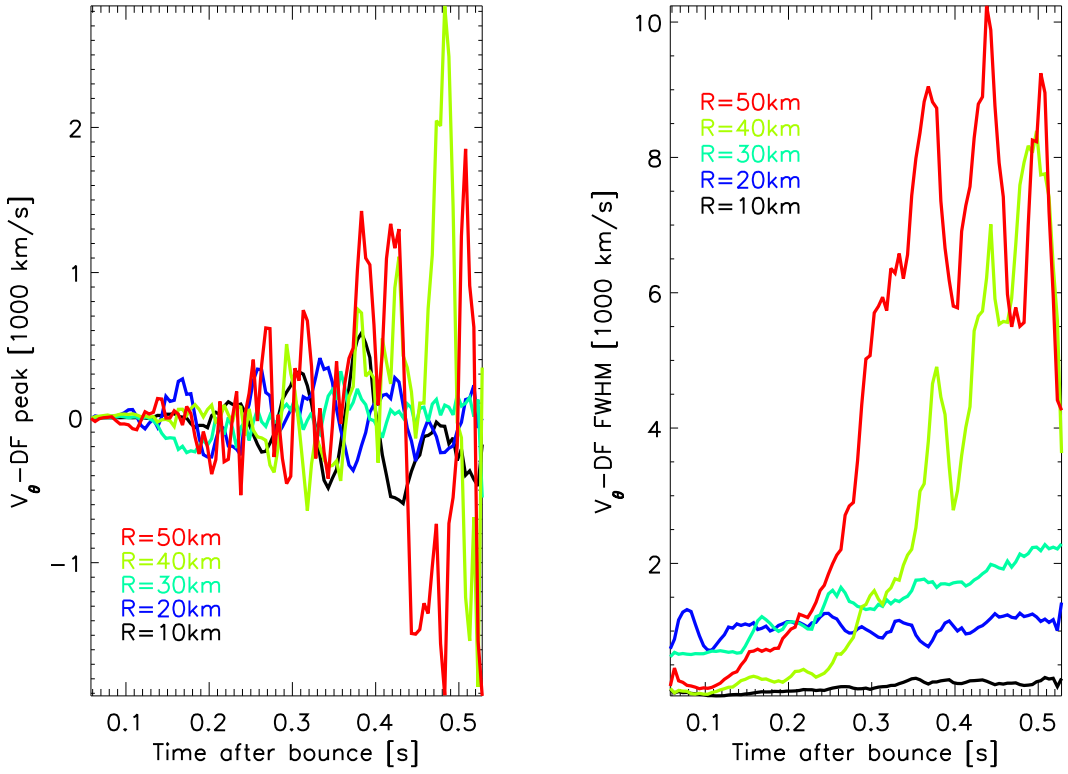


FIG. 7.— Same as Fig. 6, but for the latitudinal velocity, $V_\theta$.

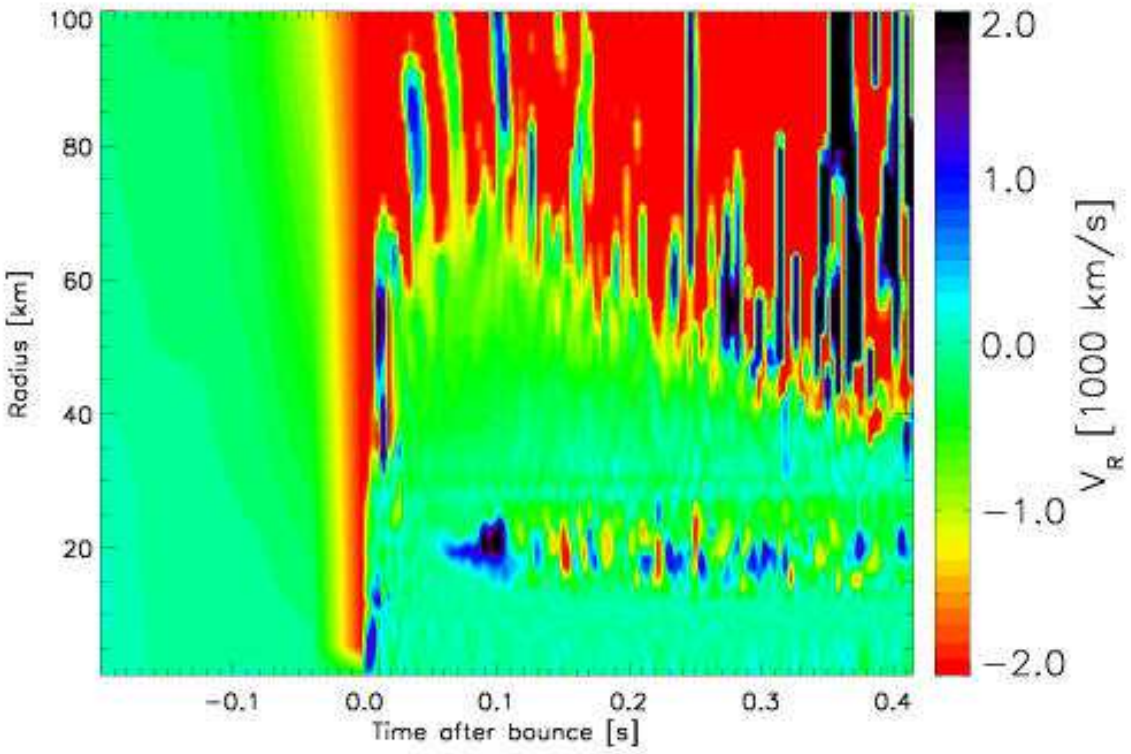


FIG. 8.— Color map of the radial velocity $V_R$ as a function of time after bounce and radius, along the equatorial direction. The green regions denote relatively quiescent areas. The inner region of the outer convective zone (Region D) is the predominately red zone; the horizontal band near ∼20 km is Region B, where isolated PNS convection obtains. See Buras et al. (2005) for a similar plot and the text for details.

Given a variable $x$ and a function $f(x)$, one can compute, for a range of values $y$ encompassing the extrema of $f(x)$, the new function

$$g(f(x), y) \propto \exp\left[-\left(\frac{y - f(x)}{\sqrt{2}\sigma}\right)^2\right],$$

where $\sigma = \sqrt{< f^2(x) >_x - < f(x) >_x^2}$ and $<>_x$ is to be understood as an average over $x$. We then construct the new function:

$$h(y) =< g(f(x), y) >_x .$$

Here, to highlight the key characteristics of various fluid quantities, we extract only the $y$ value $y_{\rm peak}$ at which $h(y)$ is maximum, *i.e.*, the most representative value $f(x)$ in our sample over all $x$ (akin to the mean), and the typical scatter around that value, which we associate with the Full Width at Half Maximum (FWHM) of the Gaussian-like distribution.

In Figs. 6-7 and 10-11, we plot such peak and FWHM values at selected radii within the PNS, each lying in one of the Regions A, B, C, or D. As in Fig. 5, we select a broader time coverage, from 50 ms to 530 ms past core bounce, in order to give a clear perspective of the long-term evolution of the PNS. Figure 6 shows the radial-velocity at the peak (left panel) and FWHM (right panel) of the radial-velocity distribution function. The black, blue, and turquoise curves (corresponding to radii interior to 30 km) are similar, being close to zero for both the peak and the FWHM. In contrast, the green and red curves (corresponding to radii above 30 km) show a DF with a strongly negative peak radial velocity, even more so at later times, while the FWHM follows the same evolution (but at positive values). This is in conformity with the previous discussion. Above 30-40 km (Region D), convection underneath the shocked region induces large-scale upward and downward motions, with velocities of a few 1000 km s$^{-1}$, but negative on average, reflecting the continuous collapse of the progenitor mantle (Fig. 5). Below 30 km, there is no sizable radial flow of material biased towards inflow, on average or at any time. This region is indeed quite dynamically decoupled from the above regions during the first ∼300 ms, in no obvious way influenced by the fierce convection taking place underneath the shocked region. Turning to the distribution function of the latitudinal velocity (Fig. 7), we see a similar dichotomy between its peak and FWHM at radii below and above 30 km. At each radius, $V_\theta$ is of comparable magnitude to $V_r$, apart from the peak value which always averages to zero even at larger radii (40 and 50 km). This makes sense, since no body-force operates continuously pole-ward or equator-ward - the gravitational acceleration acts mostly radially. Radial- and latitudinal-velocity distribution functions are, therefore, strikingly similar at 10, 20, and 30 km, throughout the first 530 ms after core bounce, quite unlike the above layers, where the Mach numbers eventually reach close to unity between 50–100 km (Fig. 4).

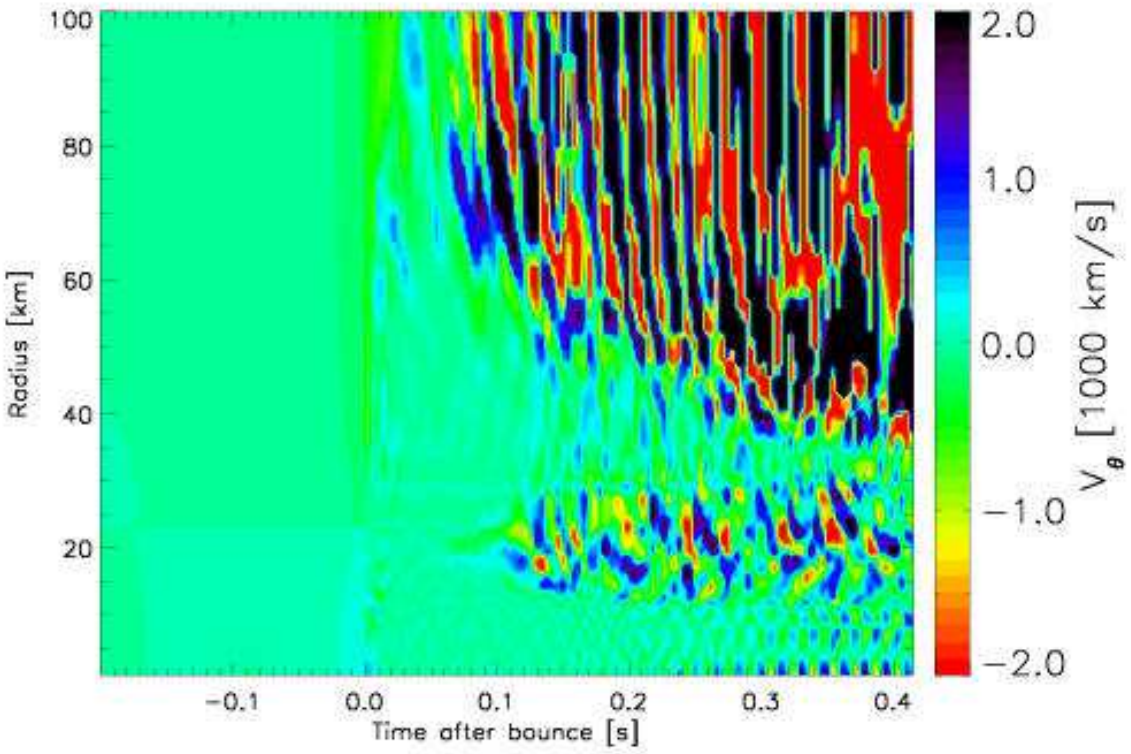


FIG. 9.— Same as Fig. 8, but for the latitudinal velocity ($V_\theta$). Note the gravity waves excited between 25–35 km, more visible in this image of the latitudinal velocity than in the previous figure for the radial velocity.

In Figs. 8–9, we complement the previous two figures by showing the temporal evolution of the radial and latitudinal velocities, using a fine sampling of half a millisecond, along the equatorial direction and over the inner 100 km. To enhance the contrast in the displayed properties, we cover the entire evolution computed with VULCAN/2D, from the start at 206 ms prior to, until 530 ms past core bounce. Note the sudden rise at ∼0.03 s prior to bounce, stretching down to radii of ∼2-3 km, before the core reaches nuclear densities and bounces. The shock wave moves out to ∼150 km (outside of the range shown), where it stalls. In the 50-100 km region along the equator, we observe mostly downward motions, which reflect the systematic infall of the progenitor envelope, but also the fact that upward motions (whose presence is inferred from the distribution function of the radial velocity) occur preferentially at non-zero latitudes. The minimum radius reached by these downward plumes decreases with time, from ∼70 km at 100 ms down to ∼40 km at 530 ms past core bounce. Note that these red and blue "stripes" are slanted systematically towards smaller heights for increasing time, giving corresponding velocities $\Delta r/\Delta t \sim -50\,\mathrm{km}/10\,\mathrm{ms} \sim -5000\,\mathrm{km\,s^{-1}}$, in agreement with values plotted in Fig. 4. The region of small radial infall above 30 km and extending to 60–35 km (from 50 to 530 ms past core bounce) is associated with the trough in the $Y_e$ profile (Fig. 4), narrowing significantly as the envelope accumulates in the interior (Fig. 5). The region of alternating upward and downward motions around 20 km persists there at all times followed, confirming the general trend seen in Figs. 6-7. The inner 10 km (Region A) does not show any appreciable motions at any time, even with this very fine time sampling. The latitudinal velocity displays a similar pattern (Fig. 9) to that of the radial velocity, showing time-dependent patterns in the corresponding regions. However, we see clearly a distinctive pattern after 100 ms past bounce and above ∼50 km, recurring periodically every ∼15 ms. This timescale is comparable to the convective overturn time for downward/upward plumes moving back and forth between the top of Region C at ∼50 km and the shock region at 150 km, with typical velocities of $5000\,\mathrm{km\,s^{-1}}$, *i.e.* $\tau \sim 100\mathrm{km}/5000\,\mathrm{km\,s^{-1}} \sim 20$ ms. In Region C, at the interface between the two convective zones B and D, the latitudinal velocity $V_\theta$ has a larger amplitude and shows more time-dependence than the radial velocity $V_r$ in the corresponding region. Interestingly, the periodicity of the patterns discernable in the $V_\theta$ field in Region C seems to be tuned to that in the convective Region D above, visually striking when one extends the slanted red and blue "stripes" from the convective Region D downwards to radii of ∼30 km. This represents an alternative, albeit heuristic, demonstration of the potential excitation of gravity waves in Region C by the convection occurring above (see §4.3).

We show the distribution function for the entropy in Fig. 10. Again, we see both in the entropy at the peak and the FWHM the dichotomy between the inner 30 km with low values, and the layers above, with much larger values for both. All radii within the PNS start, shortly

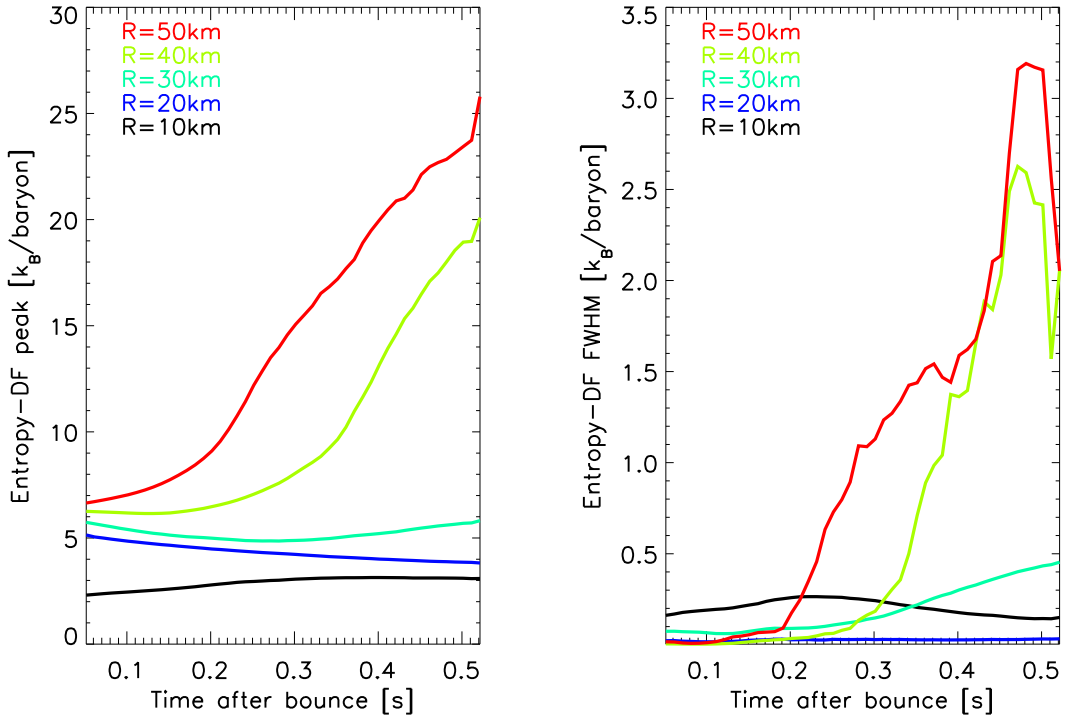


FIG. 10.— Time evolution after bounce, at selected radii, of the entropy at the peak (left) and FWHM (right) of the entropy distribution function.

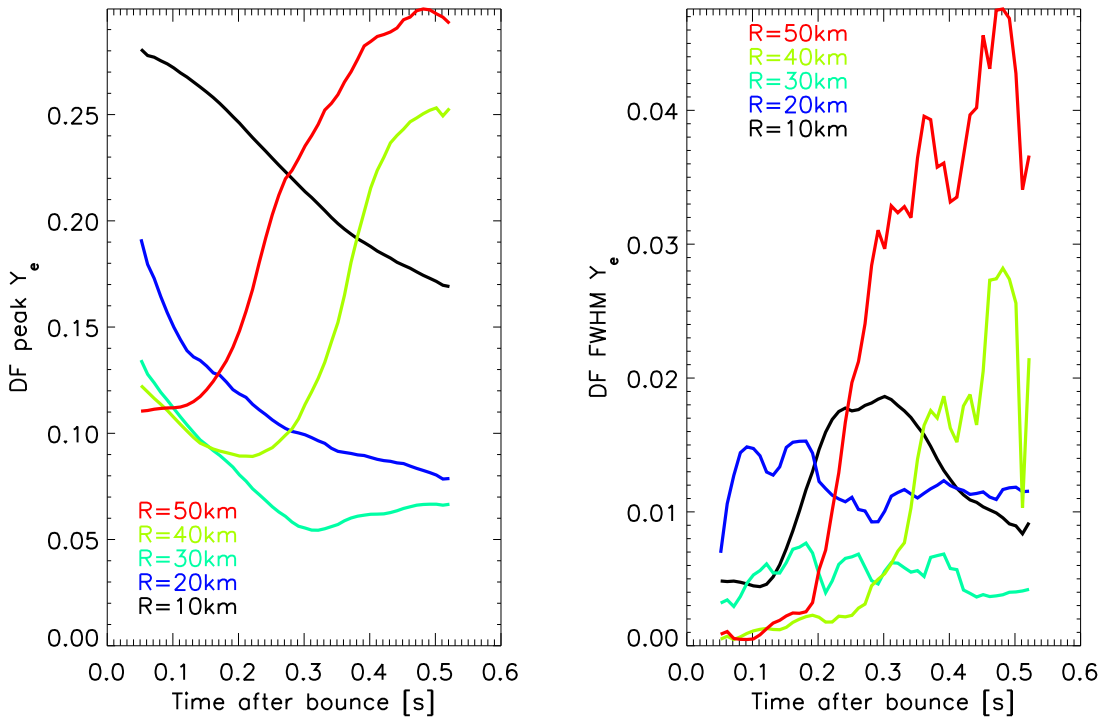


FIG. 11.— Same as Fig. 10, but for the electron fraction $Y_e$.

after core bounce (here, the initial time is 50 ms), with similar values, around 5-7 $k_B$/baryon. Below 20 km, convective motions homogenize the entropy, giving the very low scatter, while the relative isolation of these regions from the convection and net neutrino energy deposition above maintains the peak value low. Outer regions (above 30 km) are considerably mixed with accreting material, enhancing the entropy considerably, up to values of 20-30 $k_B$/baryon.

To conclude this descriptive section, we show in Fig. 11 the distribution function for the electron fraction. The dichotomy reported above between different regions is present here. Above ∼30 km, the $Y_e$ increases with time as fresh material accretes from larger radii, while below this limit, the absent or modest accretion cannot compensate for the rapid electron capture and neutrino losses. Indeed, the minimum at 30 km and 300 ms corresponds roughly with the position of the neutrinosphere(s) at late times, which is then mostly independent of neutrino energy (§4).

## 4. PROTONEUTRON STAR CONVECTION, DOUBLY-DIFFUSIVE INSTABILITIES, AND GRAVITY WAVES

In this section, we connect the results obtained for our baseline model to a number of potential modes and instabilities that can arise within or just above the PNS (here again, we focus on the innermost 50–100 km), all related to the radial distribution of entropy and lepton number (or electron) fraction. Instead of a stable combination of negative entropy gradient and positive $Y_e$ gradient in the PNS, the shock generated at core bounce leaves a positive entropy gradient in its wake, while the concomitant deleptonization due to neutrino losses at and above the neutrinosphere establishes a negative $Y_e$ gradient. This configuration is unstable according to the Ledoux criterion and sets the background for our present discussion of PNS convection and motions.

### 4.1. *Protoneutron Star Convection*

In the preceding sections, we have identified two regions where sizable velocities persist over hundreds of milliseconds, associated with the intermediate Region B (covering the range 10–20 km) and the outer Region D considered here (above ∼50 km). The latter is the region of advection-modified, neutrino-driven turbulent convection bounded by the shock wave. While this region does not directly participate in the PNS convection, it does influence the interface layer (Region C) and excites the gravity waves seen there (§4.3).

At intermediate radii (10–20 km, Region B), we have identified a region of strengthening velocity and vorticity, with little net radial velocity ($\leq 100\,\mathrm{km\,s^{-1}}$) at a given radius when averaged over all directions. In other words, significant motions are seen, but confined within a small region of modest radial extent of 10-20 km at most. As clearly shown in Fig. 4, this region has a rather flat entropy gradient, which cannot stabilize the steep negative–$Y_e$ gradient against this inner convection. This configuration is unstable according to the Ledoux criterion and had been invoked as a likely site of convection (Epstein 1979; Lattimer & Mazurek 1981; Burrows 1987). It has been argued that such convection, could lead to a sizable advection of neutrino energy upwards, into regions where neutrinos are decoupled from the matter (*i.e.*, with both low absorptive and scattering opacities), thereby making promptly available energy which would otherwise have diffused out over a much longer time.

The relevance of any advected flux in this context rests on whether the neutrino energy is advected from the diffusive to the free-streaming regions, *i.e.*, whether some material is indeed dredged from the dense and neutrino-opaque core out to and above the neutrinosphere(s). In Fig. 12, we show the energy-dependent neutrinospheric radii at four selected times past core bounce (50, 100, 200, and 300 ms) for the three neutrino "flavors" ($\nu_e$, solid line; $\bar{\nu}_e$, dotted line; "$\nu_\mu$", dashed line). At 15 MeV, near where the $\nu_e$ and $\bar{\nu}_e$ energy distributions at infinity peak, matter and neutrinos decouple at a radius of ∼80 km at $t = 50$ ms, decreasing at later times to ∼30 km. Note that the neutrinospheric radius becomes less and less dependent on the neutrino energy as time proceeds, which results from the steepening density gradient with increasing time (compare the black and red curves in the top left panel of Fig. 4). This lower-limit on the neutrinospheric radius of 30 km is to be compared with the 10–20 km radii where PNS convection obtains. The "saddle" region of very low $Y_e$ at ∼30 km, which harbors a very modest radial velocity at all times and, thus, hangs steady, does not let any material penetrate through. Figure 13 depicts the neutrino luminosities until 300 ms after bounce and shows that there are only slight bumps in the $\bar{\nu}_e$ and "$\nu_\mu$" luminosities at early times, and no perceptible bump in the $\nu_e$ luminosity (as compared to the corresponding neutrino luminosity profiles obtained, e.g., with the 1D radiation hydrodynamics code SESAME; Thompson et al. 2003). As a result, we find that PNS convective motions do not appreciably enhance the $\nu_e$ neutrino luminosity, and that they can enhance the $\bar{\nu}_e$ and "$\nu_\mu$" luminosities by no more than ∼15% and ∼30%, respectively, during the first post-bounce ∼100 ms. Afterwards, the optical depth barrier between inner PNS convection and the neutrinospheres effectively isolates one from the other, terminating even this modest enhancement. From the above discussion, we conclude that there is no sizable or long-lasting convective boost to the $\nu_e$ and $\bar{\nu}_e$ neutrino luminosities of relevance to the neutrino-driven supernova model, and that what boost there is is shut off within the first ∼100 ms of bounce.

### 4.2. *Doubly-diffusive instabilities*

When the medium is stable under the Ledoux criterion, Bruenn, Raley, & Mezzacappa (2005) argue for the potential presence in the PNS of doubly-diffusive instabilities associated with gradients in electron fraction and entropy. Whether doubly-diffusive instabilities occur is contingent upon the diffusion timescales of composition and heat, mediated in the PNS by neutrinos. Mayle & Wilson (1988) suggested that so-called "neutron fingers" existed in the PNS, resulting from the fast transport of heat and the slow-equilibration transport of leptons. This proposition was rejected by Bruenn & Dineva (1996), who argued that these rates are in fact reversed for two reasons. Energy transport by neutrinos, optimal in principle for higher-energy neutrinos, is less impeded by material opacity at lower neutrino en-

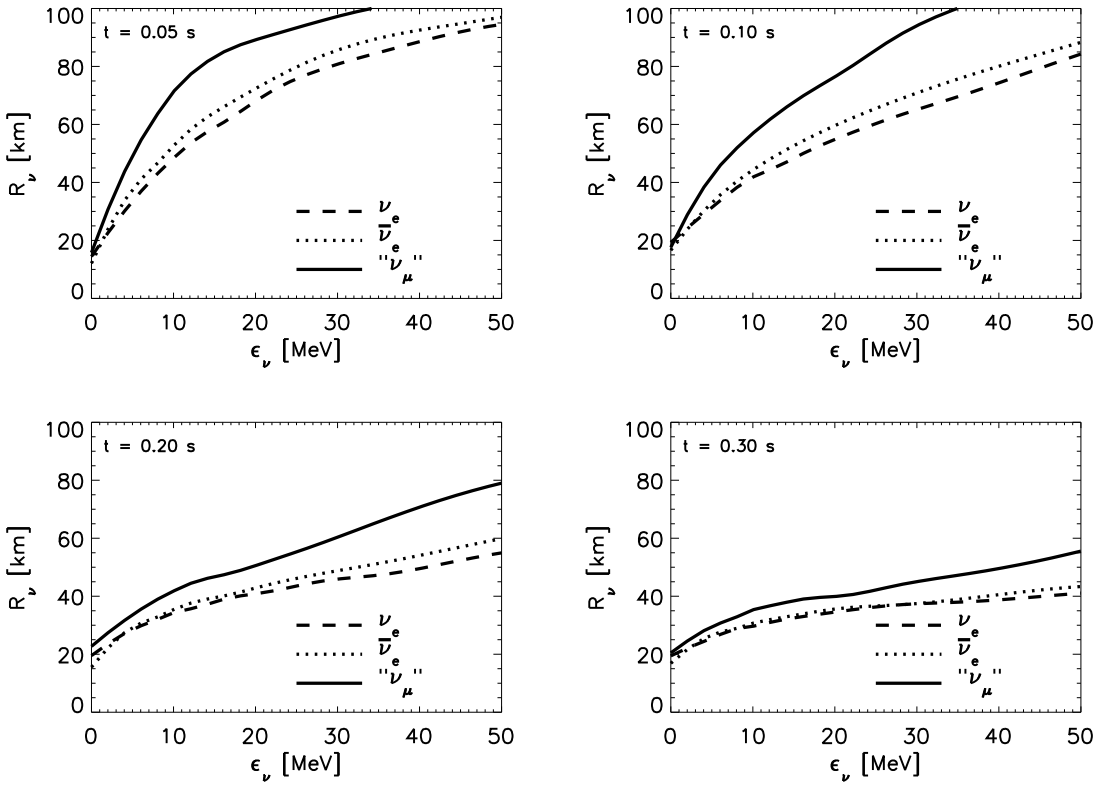


FIG. 12.— Neutrino energy dependence of neutrinosphere radii at four selected times past core bounce ($t = 50$ ms: top left; $t = 100$ ms: top right; $t = 200$ ms: bottom left; $t = 300$ ms: bottom right) for the three neutrino "flavors" ($\nu_{\rm e}$, solid line; $\bar{\nu}_{\rm e}$, dotted line; "$\nu_\mu$", dashed line) treated in our 16-energy-group baseline simulation.

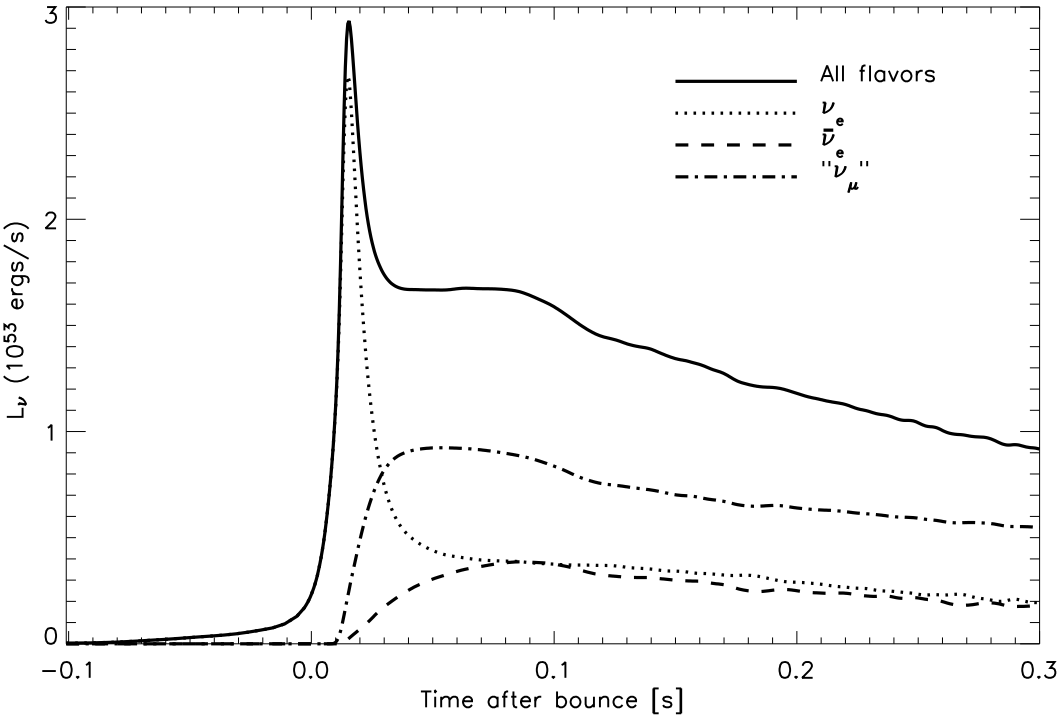


FIG. 13.— Time evolution of the neutrino luminosity, free-streaming through the outer grid radius at 3800 km, for the three neutrino "flavors" ($\nu_{\rm e}$, dotted line; $\bar{\nu}_{\rm e}$, dashed line; "$\nu_\mu$", dash-dotted line), as well as the sum of all three contributions (solid line), for our 16-energy-group baseline model. The time sampling is every 5 ms until $t = -6$ ms, and every 0.5 ms for the remaining of the simulation, where we have defined $t = 0$ as the time of hydrodynamical bounce.

ergy. Moreover, because lepton number is the same for electron/anti-electron neutrinos *irrespective* of their energy, lepton transport is faster than that of heat. This holds despite the contribution of the other neutrino types (which suffer lower absorption rates) to heat transport.

Despite this important, but subtle, difference in diffusion timescales for thermal and lepton diffusion mediated by neutrinos, the presence of convection within the PNS, which operates on much smaller timescales (*i.e.*, $\sim$1 ms compared to $\sim$1 s), outweighs these in importance. In the PNS (a region with high neutrino absorption/scattering cross sections), the presence of convection operating on timescales of the order of a few milliseconds seems to dominate any doubly-diffusive instability associated with the transport of heat and leptons by neutrinos. Furthermore, and importantly, we do not see overturning motions in regions not unstable to Ledoux convection. Hence, we do not, during these simulations, discern the presence of doubly-diffusive instabilities at all. This finding mitigates against the suggestion that doubly-diffusive instabilities in the first 300-500 milliseconds after bounce might perceptively enhance the neutrino luminosities that are the primary agents in the neutrino-driven supernova scenario.

### 4.3. *Gravity waves*

We have described above the presence of a region (C) with little or no inflow up to 100–300 ms past core bounce, which closely matches the location of minimum $Y_e$ values in our simulations, whatever the time snapshot considered. At such times after core bounce, we clearly identify the presence of waves at the corresponding height of $\sim$30 km, which also corresponds to the surface of the PNS where the density gradient steepens (see top-left panel of Fig. 4). As shown in Fig. 12, as time progresses, this steepening of the density profile causes the (deleptonizing) neutrinosphere to move inwards, converging to a height of $\sim$30-40 km, weakly dependent on the neutrino energy.

To diagnose the nature and character of such waves, we show in Fig. 14 the fluctuation of the latitudinal velocity (subtracted from its angular average), as a function of time and latitude, and at a radius of 35 km. The time axis has been deliberately reduced to ensure that the region under scrutiny does not move inwards appreciably during the sequence (Fig. 5). Taking a slice along the equator, we see a pattern with peaks and valleys repeated every $\sim$10–20 ms. We provide in Fig. 15 the angular-averaged temporal power spectrum of the latitudinal velocity (minus the mean in each direction). Besides the peak frequency at 60 Hz ($P$ $\sim$16.7 ms), we also observe its second harmonic at $\sim$120 Hz ($P$ $\sim$8.3 ms) together with two larger frequencies at $\sim$150 Hz ($P$ $\sim$6.7 ms) and $\sim$190 Hz ($P$ $\sim$5.2 ms).

Geometrically, as was shown in Figs. 1-3, the radial extent of the cavity where these waves exist is very confined, covering no more than 5–10 km around 35 km (at $\sim$200 ms). In the lateral direction, we again perform a Fourier transform of the latitudinal velocity, this time subtracted from its angle average. We show the resulting angular power spectrum in Fig. 16 with a maximum at a scale of 180° (the full range), a secondary maximum near $\sim$45°, and power down to $\sim$30°. There is essentially no power on smaller scales, implying a much larger extent of the waves in the lateral direction than in the radial direction. We also decompose such a latitudinal velocity field into spherical harmonics in order to extract the coefficients for various l-modes. We show the results in Fig. 17, displaying the time-evolution of the coefficients for $l$ up to 3, clearly revealing the dominance of $l$ =1 and 2.

These characteristics are typical of gravity waves, whose horizontal $k_h$ and vertical $k_r$ wavenumbers are such that $k_h/k_r \ll 1$. Moreover, the time frequency shown in (Fig. 15) corresponds very well to the frequency of the large-scale overturning motions occurring in the layers above, *i.e.*, $\nu_{\rm conv} \sim v_{\rm conv}/H_{\rm conv} \sim$ 100Hz, since typical velocities are of the order of 5000 km s$^{-1}$and $\Delta r$ between the PNS surface and the stalled shock is about 100 km. The behavior seen here confirms the analysis of Goldreich & Kumar (1990) on (gravity-) wave excitation by turbulent convection in a stratified atmosphere, with gravity waves having properties directly controlled by the velocity, size, and recurrence of the turbulent eddies generating them.

## 5. SUMMARY AND CONCLUSIONS

In this paper, we have presented results from multi-dimensional radiation hydrodynamics simulations of proto-neutron star (PNS) convection, providing support for the notion that large-scale overturn of core regions out to and above the neutrinosphere does not obtain. Furthermore, the restricted convection is confined to a shell; no significant amount of neutrino energy from the diffusive inner regions makes it into the outer regions where neutrinos decouple from matter, thereby leaving the neutrino luminosity unchanged from the situation in which PNS convection does not occur.

We document our results by showing the spatial and time evolution for various thermodynamic and hydrodynamic quantities, with 1) stills sampling the first 300 ms past core bounce, 2) distribution functions, 3) time series, and 4) frequency spectra. In all simulations performed, convection occurs in two distinct regions that stay separate. While convection in the outer region shows *negative* average radial-velocities, implying systematic net accretion, it is associated in the inner region (radius less than 30 km) with zero time- and angle-averaged velocities. In the interface region between the two convection zones lies a region where the radial velocity at any time and along any direction is small. This effectively shelters the inner PNS from fierce convective motions occurring above 30 km during these epochs. In this interface region, we identify the unambiguous presence of gravity waves, characterized with periods of 17 ms and 8 ms, latitudinal wavelengths corresponding to 30-180° (at 35 km), and a radial extent of no more than 10 km.

The neutrinosphere radii, being highly energy dependent 50 ms after bounce (from 20 to $\geq$100 km over the 1–200 MeV range), become weakly energy-dependent 300 ms after bounce (20 to 60 km over the same range). At 15 MeV where the emergent $\nu_{\rm e}/\bar{\nu}_{\rm e}$ energy spectra peak at infinity, neutrinospheres shrink from $\sim$80 km (50 ms) down to $\sim$40 km (300 ms). This evolution results primarily from the mass accretion onto the cooling PNS, the cooling and neutronization of the accreted material, and the concomitant steepening of the density gradient.

Importantly, the locations of the $\nu_e$ neutrinospheres

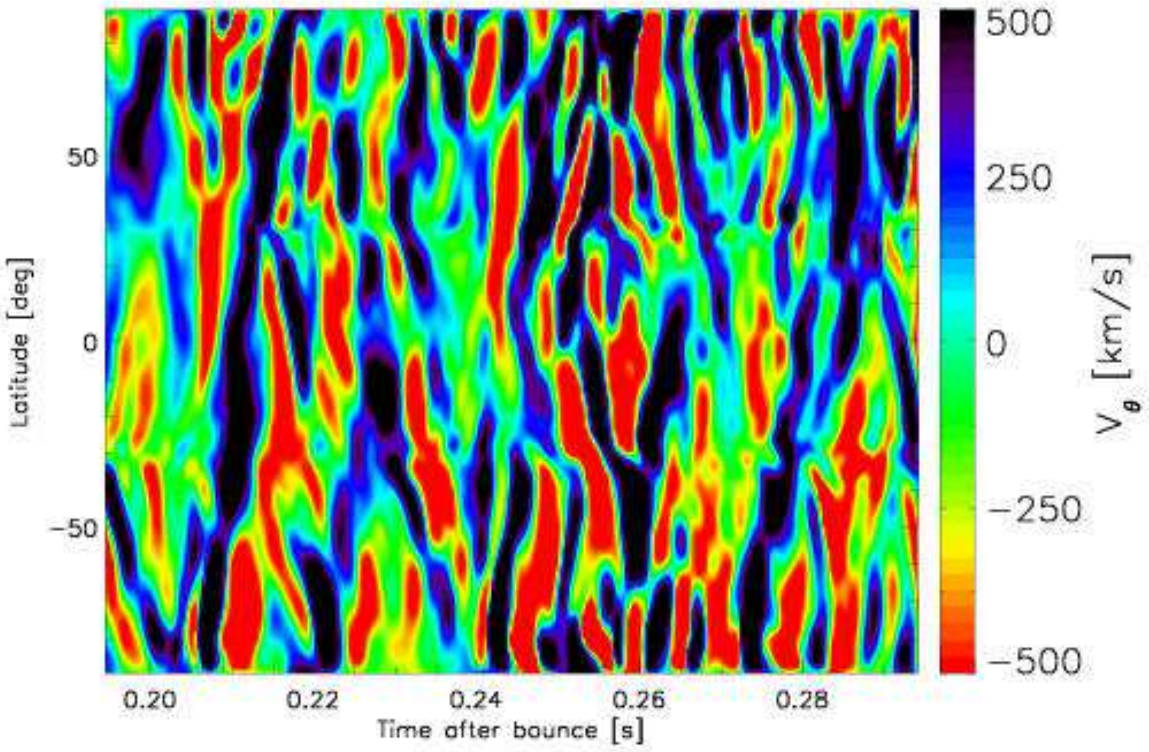


FIG. 14.— Color map of the latitudinal velocity ($V_\theta$) as a function of time after bounce and latitude, at a radius of 35 km. We restrict the time range to ∼100 ms to most effectively capture the gravity modes. Due to accretion/compression, the corresponding region recedes to greater depths with increasing time.

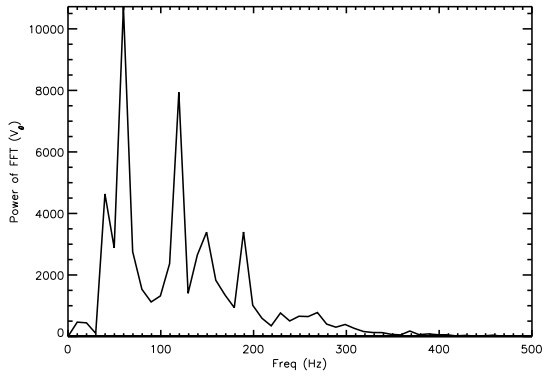


FIG. 15.— Temporal spectrum of the latitudinal velocity ($V_\theta$) at a radius of 35 km, averaged over all directions, built from a sample of 201 frames equally spaced over the range 0.194–0.294 s past core bounce.

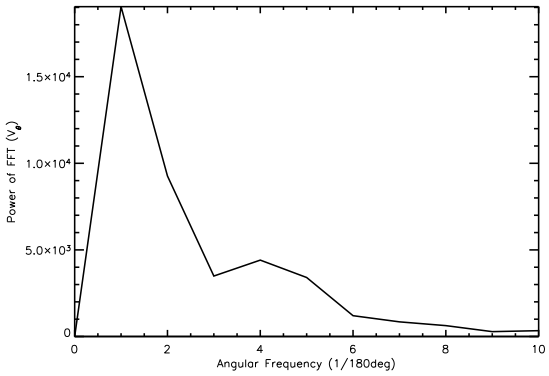


FIG. 16.— Angular spectrum of the Fourier Transform of the latitudinal velocity ($V_\theta$) at a radius of 35 km, averaged over all times, built from a sample of 120 frames covering, with equal spacing, the angular extent of the grid.

are at all times beyond the sites of convection occurring within the PNS, found here between 10 and 20 km. As a result, there is no appreciable convective enhancement in the $\nu_e$ neutrino luminosity. While energy is advected in the first ∼100 ms to near the $\bar{\nu}_e$ and $\nu_\mu$ neutrinospheres and there is indeed a slight enhancement of as much as ∼15% and ∼30%, respectively, in the total $\bar{\nu}_e$ and $\nu_\mu$ neutrino luminosities, after ∼100 ms, this enhancement is choked off by the progressively increasing opacity barrier between the PNS convection zone and all neutrinospheres. Finally, we do not see overturning motions that could be interpreted as doubly-diffusive instabilities in regions not unstable to Ledoux convection.

We acknowledge discussions with and help from Rolf Walder, Jeremiah Murphy, Casey Meakin, Don Fisher, Youssif Alnashif, Moath Jarrah, Stan Woosley, and Thomas Janka. Importantly, we acknowledge support for this work from the Scientific Discovery through Advanced Computing (SciDAC) program of the DOE, grant

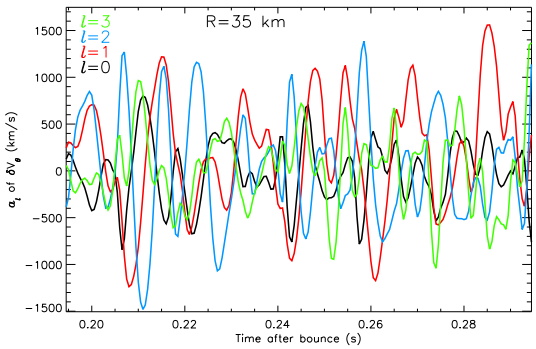


FIG. 17.— Time evolution after bounce of the spherical-harmonics coefficients for modes $l$ =0 (black), 1 (red), 2 (blue), and 3 (green) at a radius $R$ = 35 km, given by $a_l = 2\pi \int_0^\pi d\theta \sin\theta Y_l^0(\theta)\delta v_\theta(R,\theta)$.

number DE-FC02-01ER41184 and from the NSF under grant number AST-0504947. E.L. thanks the Israel Science Foundation for support under grant # 805/04, and C.D.O. thanks the Albert-Einstein-Institut for providing CPU time on their Peyote Linux cluster. We thank Jeff Fookson and Neal Lauver of the Steward Computer Support Group for their invaluable help with the local Beowulf cluster and acknowledge the use of the NERSC/LBNL/seaborg and ORNL/CCS/cheetah machines. Movies and still frames associated with this work can be obtained upon request.

## REFERENCES

Browning, M.K., Brun, A.S., & Toomre, J. 2004, ApJ, 629, 461
Bruenn, S.W. 1985, ApJS, 58, 771
Bruenn, S.W., Buchler, J.R., & Livio, M. 1979, ApJ, 234, 183
Bruenn, S.W. & Dineva, T. 1996, ApJ, 458, L71
Bruenn, S.W., Raley, E.A., & Mezzacappa, A. 2005, astro-ph/0404099
Buras, R., Rampp, M., Janka, H.-Th., & Kifonidis, K. 2005, astro-ph/0507135
Burrows, A. 1987, ApJ, 318, 57
Burrows, A., Hayes, J., & Fryxell, B.A. 1995, ApJ, 450, 830
Burrows, A. & Goshy, J. 1993, ApJ, 416, 75
Epstein, R.I. 1979, Mon. Not. R. Astro. Soc., 188, 305
Goldreich, P., & Kumar, P. 1990, ApJ, 363, 694
Janka, H.-T. & Müller, E. 1996, Astron. Astrophys. , 306, 167
Keil, W., Janka, H.-T., & Müller 1996, ApJ, 473, 111
Lattimer, J.M. & Mazurek, T.J. 1981, ApJ, 246, 955
Ledoux, P. 1947, ApJ, 105, 305
Livio, M., Buchler, J.R., & Colgate, S.A. 1980, ApJ, 238, L139
Livne, E. 1993, ApJ, 412, 634
Livne, E., Burrows, A., Walder, R., Thompson, T.A., & Lichtenstadt, I. 2004, ApJ, 609, 277
Mayle, R. & Wilson, J. R. 1988, ApJ, 334, 909
Ott, C.D., Burrows, A., Livne, E., & Walder, R. 2004, ApJ, 600, 834
Ott, C.D., Burrows, A., Thomspon, T.A., & Livne, E. 2005, submitted to ApJ
Smarr, L., Barton, S., Bowers, R.L., Wilson, J.R., 1981, ApJ, 246, 515
Swesty, F.D., & Myra, E.S. 2005, astro-ph/0506178
Swesty, F.D., & Myra, E.S. 2005, astro-ph/0507294
Thompson, T.A., Burrows, A., & Pinto, P.A. 2003, ApJ, 592, 434
Walder, R., Burrows, A., Ott, C.D., Livne, E., Lichtenstadt, I., & Jarrah, M. 2005, ApJ, 626, 317
Wilson, J.R. & Mayle, R.W., 1993, Phys. Repts., 227, 97
Woosley, S.E. & Weaver, T.A. 1995, ApJS, 101, 181